Intermittency analysis of high-lift airfoil with slat cove fillers

Hasan Kamliya Jawahar*,
University of Bristol, Bristol, United Kingdom, BS8 1TR
Stefano Meloni†,
Department of engineering , University of RomaTre, Rome, Italy, 00146
Mahdi Azarpeyvand‡,
University of Bristol, Bristol, United Kingdom, BS8 1TR
Roberto Camussi§
Department of engineering , University of RomaTre, Rome, Italy, 00146
and
Carlos R. Ilário da Silva¶
Embraer, São José dos Campos, 12227-901, Brazil

Experimental measurements were carried out to assess the aeroacoustic characteristics of 30P30N airfoil fitted with two different types of slat cove fillers at the aeroacoustic facility at the University of Bristol. The results are presented for the angle of attack $\alpha = 18°$ at a free-stream velocity of $U_\infty = 30$ m/s which corresponds to a chord-based Reynolds number of $Re_c = 7 \times 10°$. Simultaneous measurements of the unsteady surface pressure were made at several locations in the vicinity of slat cove and at the far-field location to gain a deeper understanding of the slat noise generation mechanism. The results are analyzed using a higher-order statistical approach to determine the nature of the broadband hump seen at low-frequency for the 30P30N high-lift airfoil observed in recent studies and also to further understand the tone generation mechanism within the slat cavity. A series of cross-correlation and coherence of the unsteady pressure measurements are carried out to identify and isolate the low-frequency hump. Wavelet analysis is performed to investigate the nature of the slat-wing resonant intermittent events in both time and frequency domains. The far-field noise measurement results showed that significant noise reduction can be achieved by the use of slat cove fillers. A series of far-field and near-field correlation are also presented to show the propagated noise from the slat.

Nomenclature

c	=	stowed chord length, m
c_s	=	slat chord length, m
f	=	frequency, Hz
l	=	span length, m
p'	=	fluctuation surface pressure, Pa
P_{ref}	=	reference pressure ($= 2 \times 10^{-5}$), Pa
P_{rms}	=	pressure root mean squared
Re_c	=	chord-based Reynolds number
St_s	=	slat chord-based Strouhal number, ($St_s = f \cdot c_s / U_\infty$)
U, U_∞	=	mean velocity, free-stream velocity, m/s
α	=	angle of attack, °
τ	=	time delay, s
Φ_{pp}	=	wall-pressure power spectral density, Pa^2/Hz
$\gamma^2_{p_i p_j}$	=	wall pressure coherence between transducers p_i and p_j

*Research Associate, Department of Aerospace Engineering, hasan.kj@bristol.ac.uk
†PhD Student, University of Roma Tre, stefano.meloni@uniroma3.it
‡Professor in Aeroacoustics, Department of Mechanical Engineering, m.azarpeyvand@bristol.ac.uk
§Professore di Fluidodinamica, University of RomaTre, roberto.camussi@uniroma3.it
¶Technology Development Engineer, Embraer, Sáo José dos Campos, Brazil, carlos.ilario@embraer.com.br

I. Introduction

THE extensive growth of the aircraft industry constantly demands much more efficient and quieter aircraft than the ones currently in service. The impact noise generated by aircraft during take-off and landing has come under a lot of scrutinies over the past decade especially with the increasing popularity in air travel and expanding airports. Even though the aircraft engine noise has been brought down substantially by the use of high bypass engines the airframe noise remains a major contributor to aircraft noise. In order to reduce these prominent noise sources several passive and active flow control methods have been investigated in the past it includes morphing structures [1–10], porous materials [11–13], surface treatments [14], serrations [15–17] and transverse jets [18]. The high-lift devices namely the slats and flaps are one of the major contributors to airframe noise. Their noise generation mechanism is of both broadband and narrowband in nature. Studies on conventional slat and wing configurations have shown that it mainly comprises of broadband and tonal noise components. Several studies on slat noise have shown several discrete tones at mid-frequency range [19–34]. However, their aeroacoustic mechanism is yet to be fully understood. These tonal peaks decrease with the angle of attack but their amplitude decreases with increasing slat gap and overlap [28].

Several successful studies [35–45] were carried out over the two decades to reduce the characteristic noise arising from the slat. They achieved this by enclosing the recirculation within the slat cavity. The characteristic tones from the slat are due to the feedback loop between the vortex shedding emanating from the slat cusp and its impingement on the slat lower surface. In order to eliminate this tonal noise and the broadband noise from the shear layer impingement the approach of filling the slat cavity is used. Horne *et al.* from NASA in order to eliminate the unsteady recirculation region within the slat cove tested a solid slat cove filler (SCF) and showed that it was effective in reducing broadband slat noise up to 4-5 dB [35]. Streett *et al.* further investigated and showed noise reduction to be sensitive to the angle of attack and SCF modification. The SCF modification showed a reduction of 3-5 dB over a wide spectrum [36]. Imamura *et al.* and Ura *et al.* from JAXA showed experimentally and computationally [39,40] and showed a reduction of 5 dB.

Previous studies [19–34] have showed that the strong tonal peak in the mid-frequency range ($St_s = 1 - 5$) is generated due to the flow acoustic cavity feedback mechanism of slat cove shear layer instabilities. A possible quadratic interaction between the tonal peaks has also been observed [26–30]. A spectral hump at low-frequency range ($St_s < 1$) could be observed in these studies but it is always thought to be part of the cavity feedback mechanism.

In a recent study [2], the authors showed that the first Rossiter mode is concealed within the spectral hump $0.5 < St_s < 1$ and that the source of the spectral hump is not solely due to the Rossiter modes. The Rossiter modes are due to the flow-induced oscillations from the vortex shedding and the acoustic feedback mechanism has a distinct narrowband peak. Further higher-order spectral analysis of the near field pressure fluctuations also confirmed this with strong self-interaction of the spectral hump ($0.5 < St_s < 1$) with no cross interaction, while the other narrowband peaks showed a high level of quadratic coupling and cross interaction. The results from the persistence spectrum also showed that the spectral hump ($0.5 < St_s < 1$) is not dominated over time like the other narrowband peaks, rather the energy of the broadband spectra is evenly distributed in time over the entire frequency range.

Even though several studies [35–44] have been performed to report the aerodynamic and aeroacoustic behaviour of slat cove fillers. Further fundamental understanding of the noise generation mechanism of the slat and the noise suppression mechanism of the slat cove fillers are yet to be analyzed in detail. It is well known that the source of the tonal peak is due to the Rossiter modes that arise from the interaction between the slat cusp and its trailing edge, however the source of the broadband hump at low-frequency is yet to be identified. This paper uses higher-order spectral and statistical analysis to improve the understanding of this low-frequency spectral hump and the slat noise generation mechanism. Data were analyzed providing an exhaustive intermittency characterization including spectral quantities, high order statistical moments, cross-correlations, and wavelet transform.

The paper is divided as follows: the experimental setup is reported in section II, results in terms of single and two-point statistics are reported in section III. The final remarks are in section IV.

II. Experimental Setup

A. Airfoil Setup

An aluminum 30P30N three-element high-lift airfoil with a retracted chord of $c = 0.35$ m and a span of $l = 0.53$ m was manufactured using a computer-aided numerically controlled machine. The geometrical parameters of the high-lift airfoil are shown in Fig. 1 and Table. 1. In order to maintain two-dimensionality within the slat cove and flap cove regions, no brackets were used in the spanwise direction. All the three-elements were held together by steel clamps on the sides of the airfoil. A zig-zag turbulator tape with a thickness of $h_t = 0.5$ mm and a width of $w_t = 6$ mm with a turbulator angle of 70° was used at location $x/c = -0.055$ on the pressure side of the slat surface just upstream of the slat cusp to trip the flow and induce turbulent shear layer [22]. Thorough studies on the manufactured 30P30N high-lift airfoil model were carried out at different test conditions and the results validated with existing benchmark studies [1, 2].

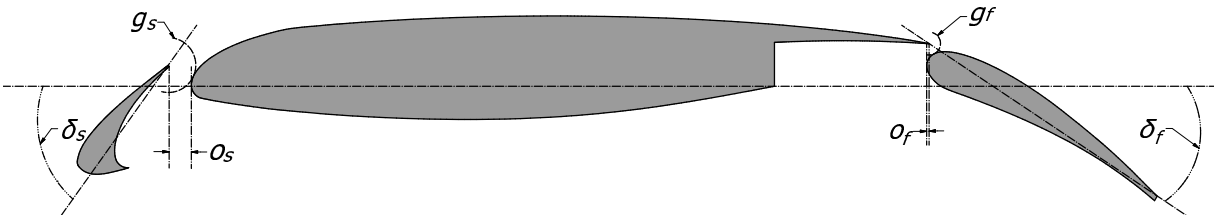

Fig. 1. Geometric parameters of the 30P30N three-element high-lift airfoil.

Table 1. Geometrical parameters in percentage of stowed airfoil chord, $c = 0.35$ m.

Slat chord	c_s	$0.15c$
Main-element chord	c_{me}	$0.83c$
Flap chord	c_f	$0.3c$
Slat deflection angle	δ_s	30°
Flap deflection angle	δ_f	30°
Slat gap	g_s	2.95%
Flap gap	g_f	1.27%
Slat overhang	o_s	−2.5%
Flap overhang	o_f	0.25%

1. Slat cove-filler Design

As part of the noise reduction study of the 30P30N airfoil, a slat cove-filler (SCF) was designed using a similar strategy introduced by Imamura *et al.* [39, 40] for experimentation purposes. Initially, preliminary RANS steady-state simulation for the Baseline case was performed at the angle of attack $\alpha = 8°$ and the slat shear layer trajectory with high TKE was used to define the shape of the SCF profile. Another configuration with a Half slat cove filler (H-SCF) was also considered, which exhibits good aerodynamic and noise reduction properties as shown computationally by Tao [44]. Both the slat cove-fillers were manufactured using 3D printing technology and was manufactured in four different sections that could be slid along the span of the slat cove.

B. Wind-Tunnel Setup

The aeroacoustic measurements were carried out at the University of Bristol Aeroacoustic Facility. It is a closed-circuit open-jet anechoic wind tunnel with a nozzle exit of 0.5 m × 0.775 m and a contraction ratio of 8.4:1. The wind tunnel is capable of velocities up to 40 m/s with turbulence levels as low as 0.25% [46]. The tests were carried out at angle of attack $\alpha = 18°$ for a free-stream velocity of $U_\infty = 30$ m/s, which corresponds to a chord-based Reynolds number of $Re_c = 7.0 \times 10^5$.

1. *Acoustic measurements and instrumentation*

FG-3329-P07 transducers from Knowles Electronics were installed on the main-element of the wing to measure the unsteady surface pressure on the 30P30N airfoil (FG1-FG5, see Table. 2). This transducer was selected for measurement as it was proven successful in previous experiments carried out by Garcia [47] on NACA 0012 airfoil. The transducer has a diameter of 2.5 mm and a height of 2.5 mm with a sensing area of 0.8 mm. The unsteady surface pressure measurements were also performed using remote sensing microphone probes made from Panasonic WM-61A microphones and 1.6 mm diameter brass tube with 0.4 mm pinholes at different streamwise locations (see Fig. 2 and Table. 2) and are connected to the pressure tap brass tube using a plastic tubing with an inner and outer diameter of 0.8 mm and 4 mm [48]. The far-field measurements were carried out using Panasonic WM-61A microphones placed at an angle of 90° at a distance of 1 m below the the slat trailing edge. The calibration of the near and far-field microphones was carried out using a pistophone calibrated G.R.A.S. 40PL microphone. The data was acquired using a National Instruments PXIe-4499 modules mounted in a National Instruments PXIe-1062Q chassis. The data for all the microphones were simultaneously collected for 120 seconds at a sampling frequency of $f_s = 2^{15}$ Hz. The power spectrum results were obtained using the power spectral density (PSD) of the pressure signals with the Hanning window and the acquired data were averaged for 220 times to yield a frequency resolution of $\Delta f = 2$ Hz. The statistics of the pressure fluctuation were investigated using the Sound Pressure Level (SPL) evaluated using the following equation:

$$SPL = 20\log_{10}\left(\frac{p_{rms}}{p_{ref}}\right), \tag{1}$$

where p_{rms} is the root-mean-square of the acoustic pressure and p_{ref} is the reference pressure that measures $p_{ref} = 20\mu Pa$. The SPL was plotted versus the Strouhal number computed as follows:

$$St_s = \frac{fc_s}{U_\infty}, \tag{2}$$

where c_s is the slat chord and U_∞ is the free-stream velocity. The results of the unsteady surface pressure auto-spectra are presented in Fig. 6 for all the remote sensors (see Table 2) and the tested slat configurations.

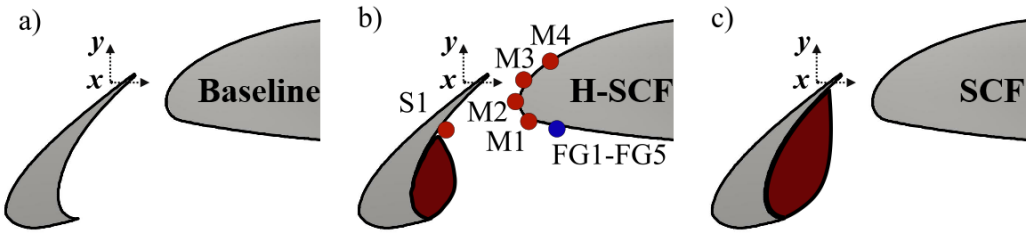

Fig. 2. Location of the unsteady pressure measurement probes a) Baseline, b) H-SCF and c) SCF.

Table 2. Streamwise and spanwise unsteady pressure measurement location on the 30P-30N airfoil.

No.	x (mm)	y (mm)	z (mm)
S1	-6.918	-11.622	265
M1	17.347	-10.019	265
M2	15.126	-5.839	265
M3	17.622	0	265
M4	23.520	5.485	265
FG1	22.414	-11.356	277
FG2	22.414	-11.356	280.6
FG3	22.414	-11.356	288.4
FG4	22.414	-11.356	301.4
FG5	22.414	-11.356	319.6

III. Results and Discussion

A. Far-field noise

The far-field noise levels for the 30P30N airfoil with various slat cove filer configurations were measured using a single Panasonic WM-61A microphone below the slat trailing edge at an angle of 90° at a distance of 1 m. The far-field pressure fluctuations were analyzed in the frequency domain using the SPL through the Eq. 1. The spectra for all the different configurations were reported in Fig. 3. Persistence of the peak close to $St_s = 1.6$ and $St_s = 3.2$ are detected for both near field and far-field. The results from the near-field region at location FG1 is presented in Fig. 3(b). The results show a characteristic tonal peak for the Baseline configuration.

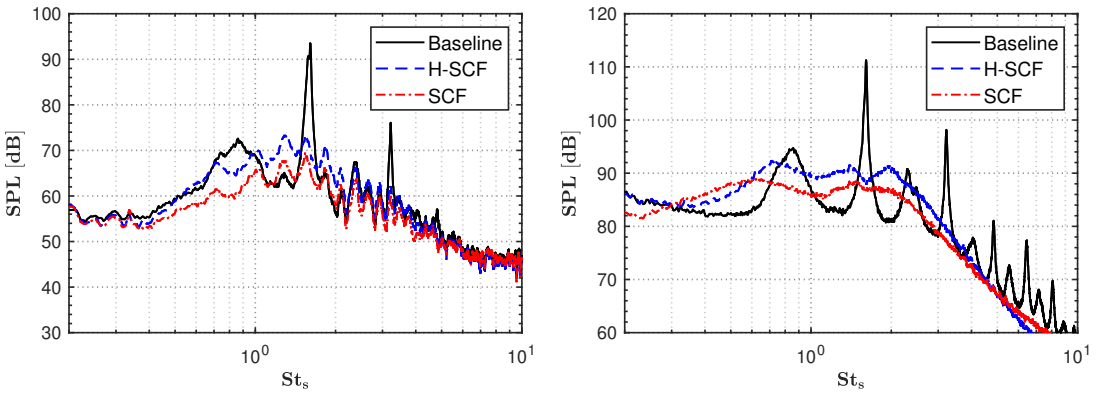

a) Far-field, FF1 b) Near-field, FG1

Fig. 3. Sound pressure level for all the tested configuration a) far-field measurements FF1 at 1 m below the slat trailing edge b) Near-field measurement FG1 on the main-element.

The tonal characteristics of the wall pressure spectra with multiple distinct narrowband peaks indicate the presence of cavity oscillations for the Baseline in Fig. 3. These tonal peaks were also seen in the far-field noise measurements. The tonal peaks observed are due to the flow-acoustic coupling which leads to resonance as all of them could be accurately predicted by the simplified Rossiter mode equation [21, 25, 49]. The discrete tonal frequencies due to the flow interaction with the slat, based on Terracol's study [25], can be predicted from

$$f_n = n\frac{U_\infty}{L_a}\left(\frac{1}{M + \eta_l/\kappa_v}\right). \tag{3}$$

A simplified schematic of the parameters used in Eq. 3 by Terracol *et al.* [25] are shown in Fig. 4 and the parameters used in the current study are listed in Table 3. The flow field, i.e. local flow velocity, data required for this prediction model were acquired from the PIV measurements by the authors in previous studies [1, 3, 6].

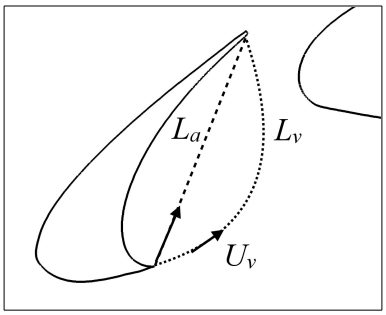

Fig. 4. Simplified schematic of the tonal frequency prediction model by Terracol *et al.* [25].

The results from the Terracol *et al.* [25] Eq. 3 are presented in Table 4. The modes are accurately predicted by Eq. 3 which confirms that the modes are generated from an acoustic feedback mechanism. The near-field results presented in Fig. 3 clearly show that the narrowband peaks from St_2 to St_6 distinct and are of high energy. Whereas, the St_1 is more of a spectral hump distributed between $St_s = 0.5 - 1$. The source of this spectral hump will be further analyzed in the following section.

Table 3. Parameters used for tonal peak frequency prediction in the present study.

α	Angle of attack	18°	units
L_v	Shear layer path length	0.037	m
L_a	Acoustic path length	0.035	m
U_v	Shear layer convection velocity	18	m/s
U_∞	free-stream velocity	30	m/s
M	free-stream Mach number	0.09	-
κ_v	$= U_v/U_\infty$	0.60	-
η_l	$= L_v/L_a$	1.06	-

Table 4. The narrow-band frequencies observed for the Baseline case in the near-field and far-field measurements at angles of attack 18°.

No.1	St_n	St_s	Description	Experiment f (Hz)	Analytical f (Hz)
1	St_1	0.85	mode 1	485.7	461.7
2	St_2	1.611	mode 2	920.6	923.3
3	St_3	2.304	mode 3	1316.6	1385
4	St_4	3.217	$= 2St_2$	1838.3	1846.6
5	St_5	3.932	$= St_3 + St_2$	2246.9	2308.3
6	St_6	4.833	$= 3St_2$	2761.7	2769.9

Wavelet decomposition for the far-field noise measurement is carried out to identify a possible influence of the hydrodynamic component propagating into the far-field region. The wavelet decomposition method employed is the WT3 [54], which is based on an iterative procedure capable of extracting the coherent structures from the pressure field. Thus the hydrodynamic component is related to the wavelet coefficients larger than the threshold level and the acoustic component to the wavelet coefficients lower than the threshold level as defined in Mancinelli *et al.* [54].

The results for the far-field spectra for all the tested 30P30N configuration after the decomposition procedure are presented in Fig. 5 for the FF1 microphone. The results for each configuration are presented for three-component of the signal, namely, original, acoustic, and the hydrodynamic component. For the Baseline and H-SCF configuration, the results clearly show for frequency between $St_s = 0.5 - 5$ the noise is dominated by both the acoustic and hydrodynamic components. The results for the Baseline and H-SCF show that for frequencies $St_s < 0.5$ and $St_s > 5$ the noise is predominantly the acoustic component. For the SCF configuration, only $St_s = 1 - 2$ is dominated by both the acoustic and hydrodynamic components, while the rest of the noise spectrum $1 > St_s > 2$ is predominantly dominated by the acoustic component. The results show that the cove filler configurations have a significant effect on the hydrodynamic component of the spectra which is reduced compared to the Baseline configuration (see Fig. 5). The wavelet decomposition method (WT3) has not proved to be efficient with tonal peaks, however, the comparative results presented here are in good agreement with the previous analysis [1, 2], which has shown that the tonal peak is related to the coherent structures, thus hydrodynamic component. Further analysis will be carried out to improve the wavelet decomposition methods to be robust and to analyze the presented near-field pressure fluctuations dominated by large peaks intermittent events.

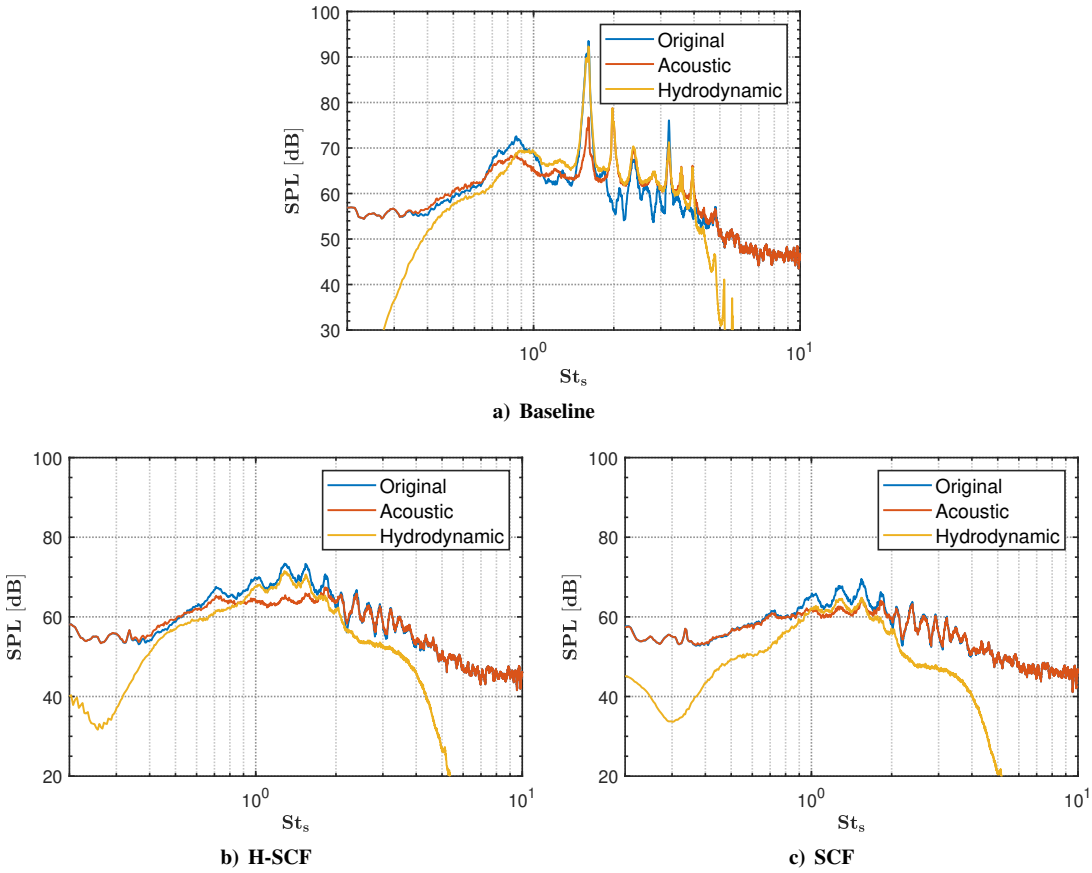

Fig. 5. Wavelet decomposition of the far-field microphone FF1 located at 1 m below the slat trailing edge.

B. Wall pressure single-point statistics

1. Power spectral density

As part of this experimental campaign in order to isolate the spectral hump at St_1, several remote sensors (M1-M4 and S1) were connected to the brass pressure ports in the vicinity of the slat cove region were used. The location of these remote sensors are detailed in Fig. 2 and Table 2. The sound pressure level for the remote sensors on the main-element M1-M4 and on the slat S1 for all the tested configurations are presented in Fig. 6. At first glance, the results for the Baseline configuration clear show several tonal peaks related to the Rossiter modes arsing from the feedback between the slat cusp and slat trailing edge. The energy of the spectra increases as the flow moves from remote sensor location M1 to M3 and decrease at M4 once the flow has passed through the slat gap. The energy of the spectra appears to be highest at M3. At location S1 on the pressure side of the slat, lower energy content is observed for the remote sensors. When considering the spectral hump St_1, it is of the same magnitude at both the locations M2 and M3, and the energy is lowest at the location M3 and slightly higher slat sensor location S1. At the slat vicinity the broadband region ($St_s < 0.5$) of the spectra is lowest at the location S1.

The use of slat cove fillers clearly eliminates the tonal peaks observed in the Baseline. The results show that the remote sensors M1 and M4 have similar spectral levels with M4 having a slightly higher spectral level at $St > 1$ for both the slat cove filler configurations. The remote sensors M2 and M3 show similar levels at $St < 1$ but at $St > 1$, M3 shows higher spectral levels both the cove filler configurations.

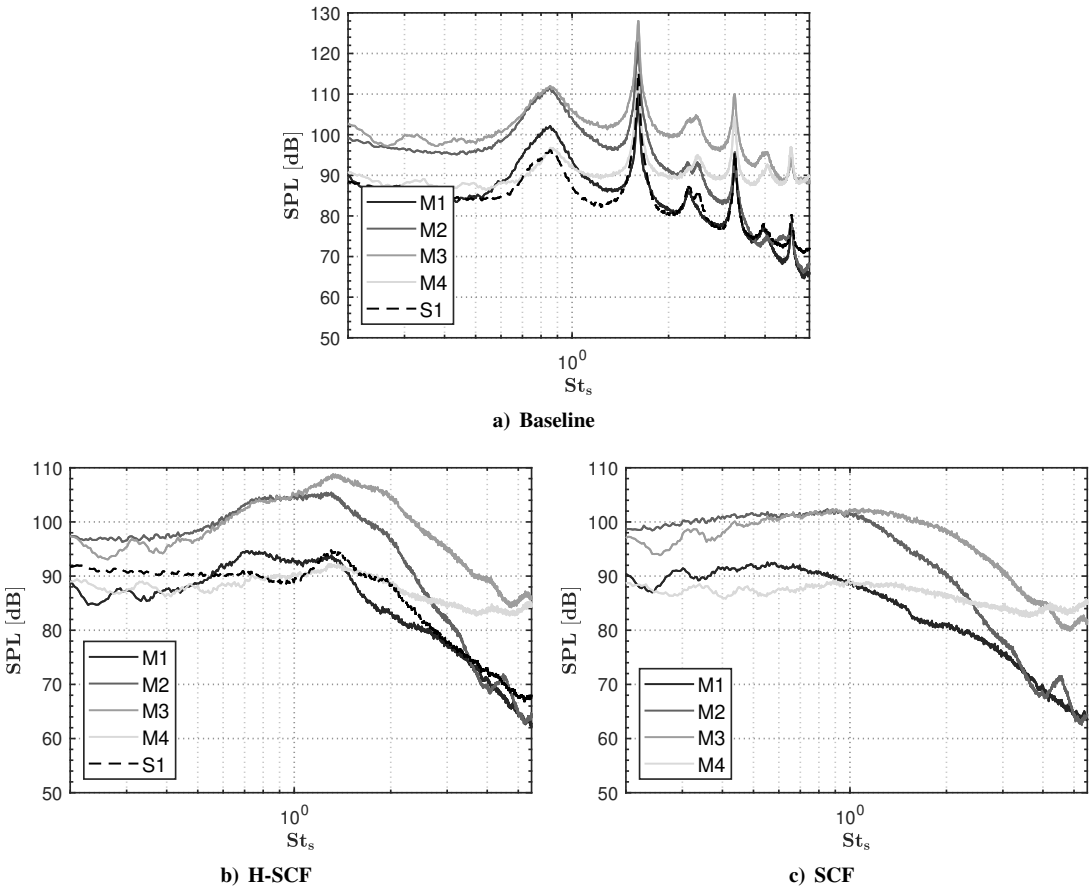

Fig. 6. Near field noise spectra for the surface pressure transducers shown in Fig. 8.

2. *Probability density function*

The wall-pressure statistics are also studied in terms of probability density function (PDF) distributions. The pressure variable is expressed in reduced form, i.e., normalized to have zero mean value and unitary standard deviation. The PDFs achieved from the experiments are compared with the standard Gaussian distribution as reported in [50]. The results for the PDF at different transducer locations are presented in Fig. 7.

The results of the PDF for the surface pressure fluctuations within the slat cove region are presented in Fig. 7. It is evident that the PDF shape for the Baseline configuration is highly dependant on the remote sensor location. At the remote sensor location M1, a quasi-Gaussian behavior is observed probably related to the slight presence of persistent events. Whereas, at location M2 and M3 the pressure events are distributed very close to the mean value. At location M4 close to the slat gap, the PDF is more inclined towards the negative pressure events. The use of slat cove fillers results in a quasi-Gaussian distribution of the pressure events, except for the location M4 where a positive tail is detected.

3. *Skewness and Kurtosis analysis*

To have a global statistical view of the fluctuating pressure field authors have reported an investigation in terms of higher-order statistical moments, like skewness (s) and kurtosis (k), computed as follows:

$$s = \frac{E[p-\mu]^3}{\sigma_p^3}, \tag{4}$$

$$k = \frac{E[p-\mu]^4}{\sigma_p^4}, \tag{5}$$

where μ is the mean of the signal p, σ_p is the standard deviation of the signal and E[·] is the expected value.

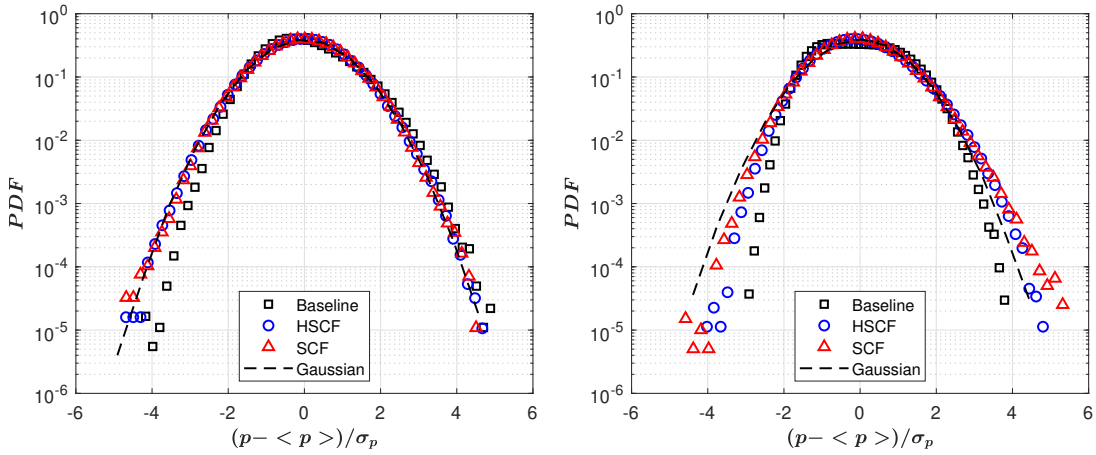

a) M1 b) M2

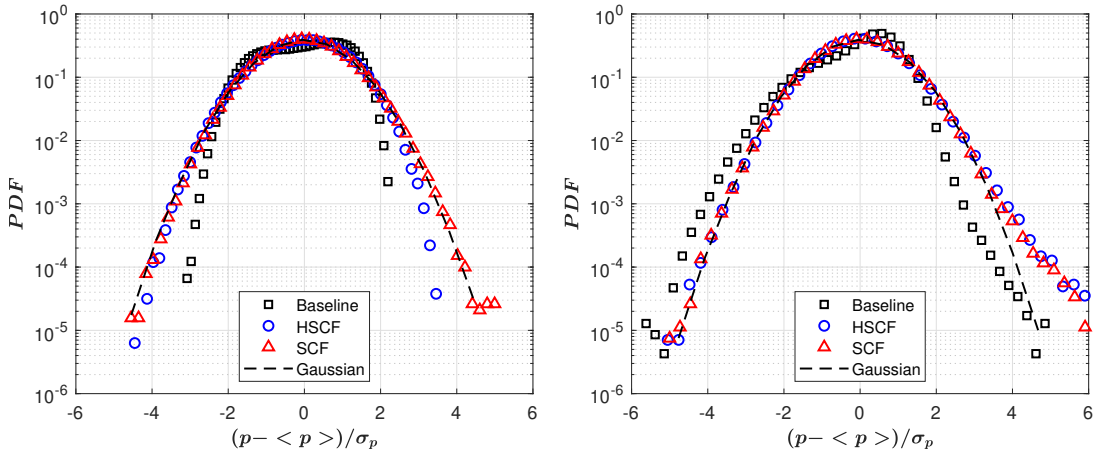

c) M3 d) M4

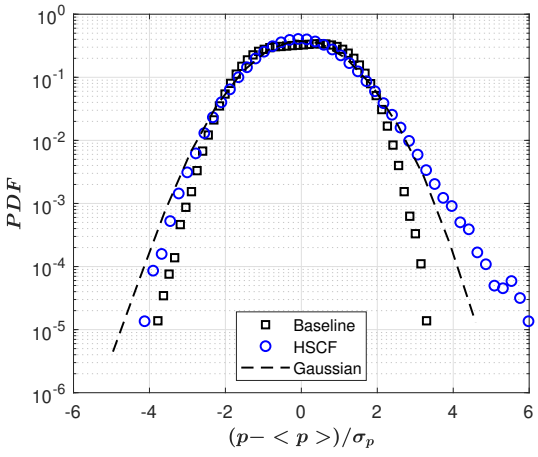

e) S1

Fig. 7. PDF for the various remote sensor on the slat and on the main-element show in Fig. 8.

The results of the skewness and kurtosis are presented in Fig. 8. If the data are fairly close to Gaussian distribution the skewness is said to be between -0.5 and 0.5 and the kurtosis to be 3. The results clearly show that for both the slat cove filler configurations the skewness and the kurtosis are within or close to the limits of a Gaussian distribution as seen in the PDFs of the pressure events. However, for the Baseline, the skewness of the pressure events at M4 is lower

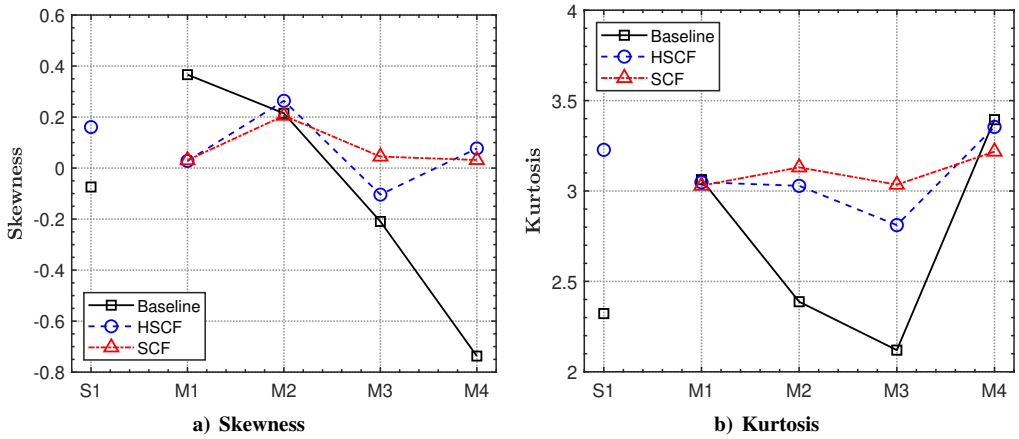

Fig. 8. Skewness and Kurtosis at various remote sensor on the main-element show in Fig. 8.

than -0.5 which suggests a negative skewness indicating that the size of the left-handed tail is larger than the right-handed tail of the distribution. For the kurtosis results the remote sensor locations M2 and M3 show values lower than three which suggests a platykurtic distribution with fewer values in the tails and fewer values close to the mean. This could be related to the presence of the persistence turbulence associated with the peak on the PSDs. Even though the skewness and kurtosis results clearly show that the flow characteristics are noticeably different at the various remote sensor locations for the Baseline, further analysis of the frequencies of interest would be required before arriving at conclusions.

C. Wall pressure two-point statistics

1. *Cross-correlation analysis*

The two-point statistics of the pressure signals were computed using the cross-correlation between two pressure transducers. In the first analysis, M1 is fixed and correlated with all the others.

The cross-correlations were computed as follows:

$$R_{p_i p_j}(\tau) = \frac{\overline{p_i(t+\tau)p_j(t)}}{p_{i_{rms}} p_{j_{rms}}}, \quad \text{for } p_i = \text{ M1 and } p_j = \text{ S1, M1, M2, M3, M4,} \tag{6}$$

where p_i and $p_{i_{rms}}$ are the surface pressure and surface pressure root mean squared of the reference transducer signals (M1), p_j and $p_{j_{rms}}$ are the surface pressure and surface pressure root mean squared of the upstream/downstream transducer signals at various location along the chord, τ is the time delay and the time average is represented by the overbar. The results of the cross-correlation of the surface pressure with reference microphone M1 at the angle of attack 18° are presented in Fig. 9.

The streamwise cross-correlation results for the remote sensors on the main-element (M1-M4) show that difference in the time lag between the various remote sensors for the Baseline configuration increases with the distance between the remote sensors. For the H-SCF configuration, the time lag between the main-element remote sensors has increased more than that of the Baseline. In the case of the SCF configuration, the time lag is further increased compared to both the Baseline and the H-SCF. The cross-correlation magnitude between the M1 and M4 has reduced substantially for the cove filler configuration. This is probably due to interference of the cove fillers on the coherent structures passing between M1 and M4. The use of cove filler appears to interfere with the turbulent structures making the cross-correlation shape larger probably due to the breaking of coherent structures.

2. *Coherence analysis*

The coherence function calculates the phase correlation between two different pressure transducers averaged over time. The coherence between the surface pressure transducers can be obtained using the following equation,

$$\gamma^2_{p_i p_j}(f) = \frac{|\,\Phi_{p_i p_j}(f)\,|^2}{\Phi_{p_i p_i}(f)\Phi_{p_j p_j}(f)} \quad \text{for } p_i = \text{ M1 and } p_j = \text{ S1, M1, M2, M3, M4,} \tag{7}$$

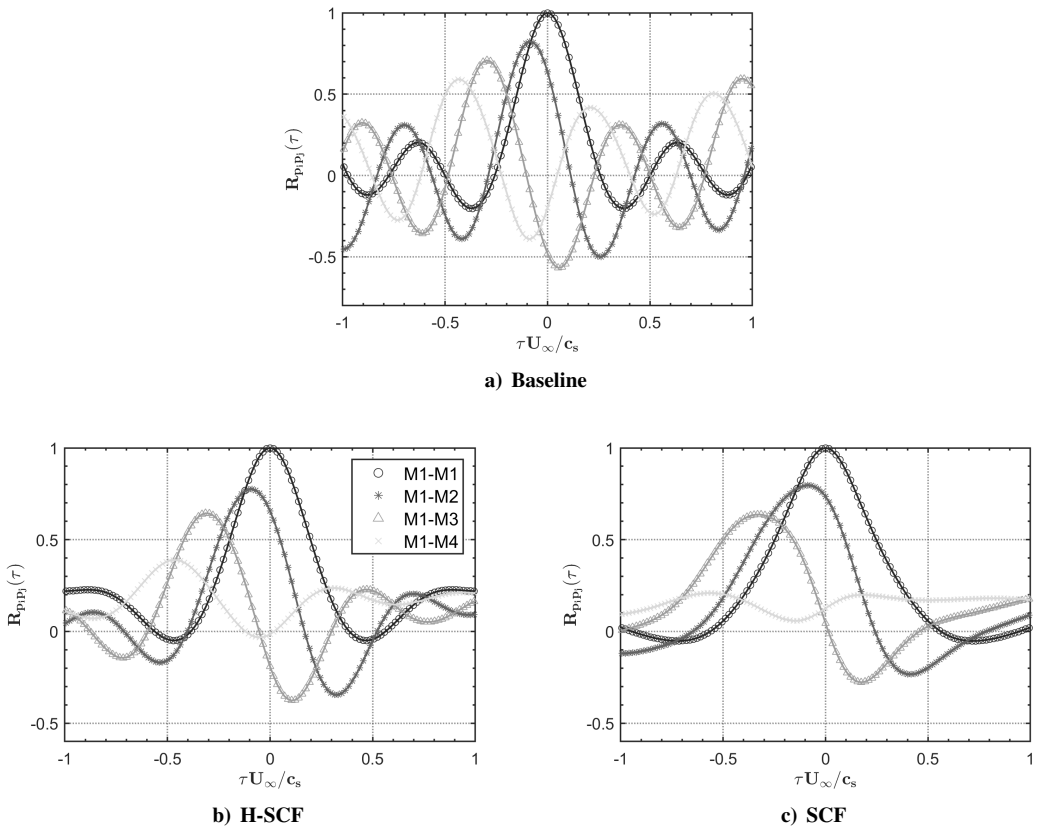

a) Baseline

b) H-SCF

c) SCF

Fig. 9. The streamwise cross-correlation of the surface pressure fluctuations between the remote sensor M1 and the following remote sensors on the main-element

where the symbol $|\square|$ denotes the absolute value, p_i is the reference transducer signal (M1), p_j is the pressure transducer signal at various location within the slat cove region and $\Phi_{p_i p_j}$ is the cross-spectral density between the two pressure signals p_i and p_j. The results for the near-field coherence of signals within the slat cavity region with M1 as reference transducers are presented in Fig. 10.

The results of the streamwise coherence of the remote sensors show a high level of coherence for the even narrowband peaks ($St_{2,4,6}$) and low coherence for the odd narrowband peaks ($St_{3,5}$) between the main-element remote sensors (M1-M4). As discussed in previous sections the spectral hump is clearly of different nature at remote sensor location M1-M2 has a high coherence level between $St_s = 0.6 - 1$, and M1-M3 between $St_s = 0.6 - 1$, whereas at location M1-M4 the high level of coherence is only between $St_s = 0.8 - 1$. This shows that even though the peak St_1 might be related to Rossiter mode but the hump itself is not caused by it. For the H-SCF and SCF configuration high coherence for $St_s < 1$ at location M1-M2 and M1-M3. Interestingly at location M1-M2 for $St_s > 2$ the SCF configuration shows higher coherence compared to the H-SCF at M1-M2, the cause of which is yet to be investigated. The coherence level at M1-M4 for the SCF configuration is lower compared to the H-SCF, however, for both the H-SCF and SCF a peak in the coherence level can be found at $St_s = 1.6$.

In order to understand the propagation effects of the wall pressure identified signatures the magnitude square coherence between wall pressure and far-field signals are presented in Fig. 11.

The results of the near to far-field coherence presented in Fig. 11 show a very high level of coherence for a series of narrowband peaks for the Baseline configuration. The coherence results are high for the even narrowband peaks ($St_{2,4,6}$) relative to the odd narrowband peaks ($St_{1,3,5}$) for all the remote sensors. A coherence level of close to 0 is detected for a wide range of frequency for both the slat cove filler configurations. For the H-SCF configuration marginally increased coherence levels can be found for two spectral humps at about $St_s = 0.5 - 1$ and at $St_s = 1.6$. The SCF configuration has the lowest coherence levels with the far-field compared to all the configurations except for a small spectral hump at about $St = 1.6$. It is noteworthy that for the SCF configuration the St_1 spectral hump has no coherence with the far-field.

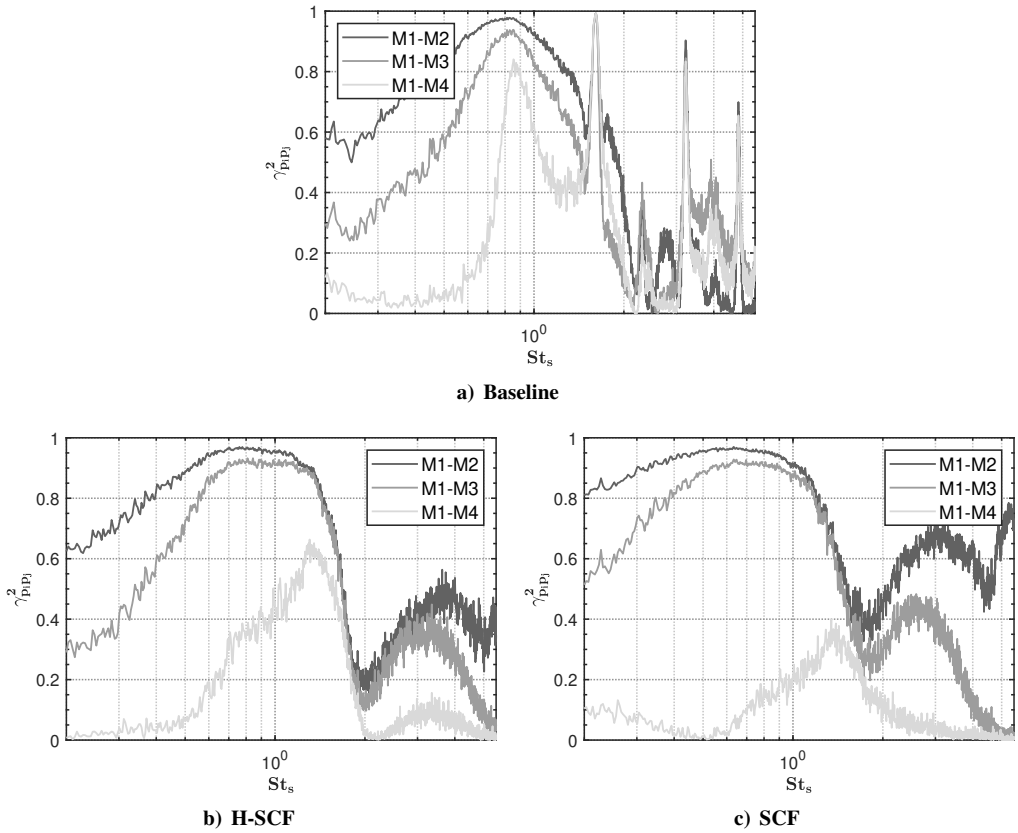

a) Baseline

b) H-SCF

c) SCF

Fig. 10. The streamwise coherence of the surface pressure fluctuations between the remote sensor M1 and the following remote sensors on the main-element.

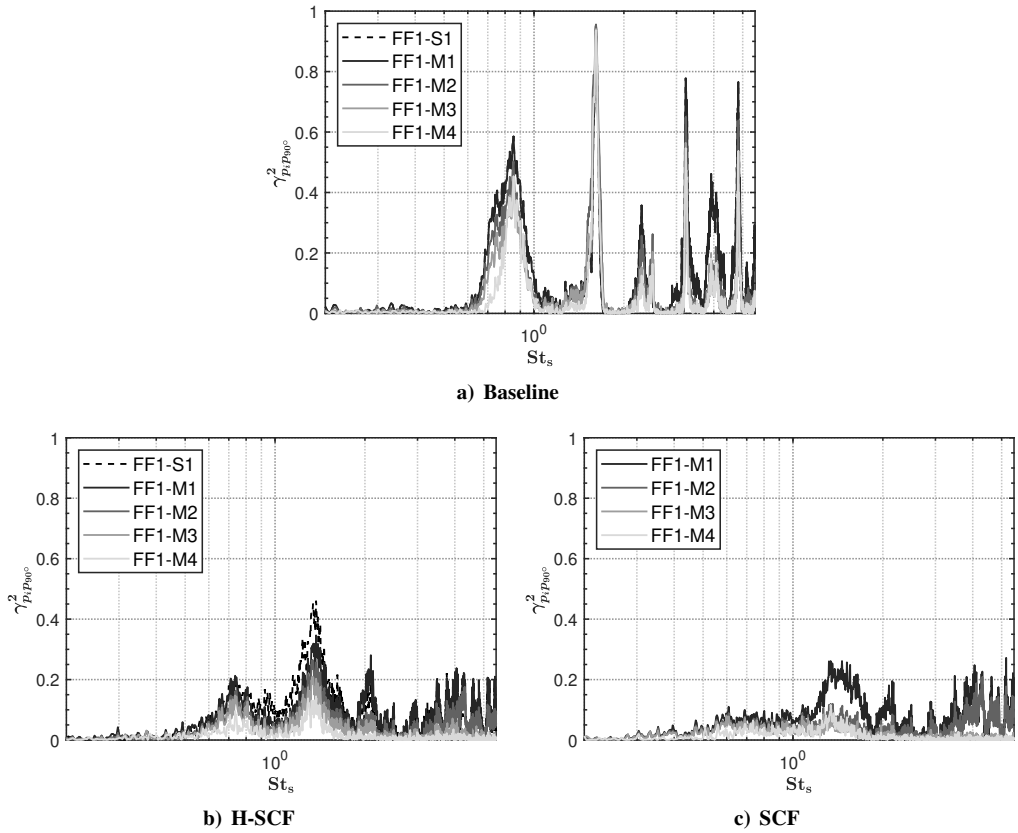

a) Baseline

b) H-SCF

c) SCF

Fig. 11. Coherence of the surface pressure fluctuations between the far-field microphone FF1 located at 1 m below the slat trailing edge and the various remote sensors on the high-lift airfoil.

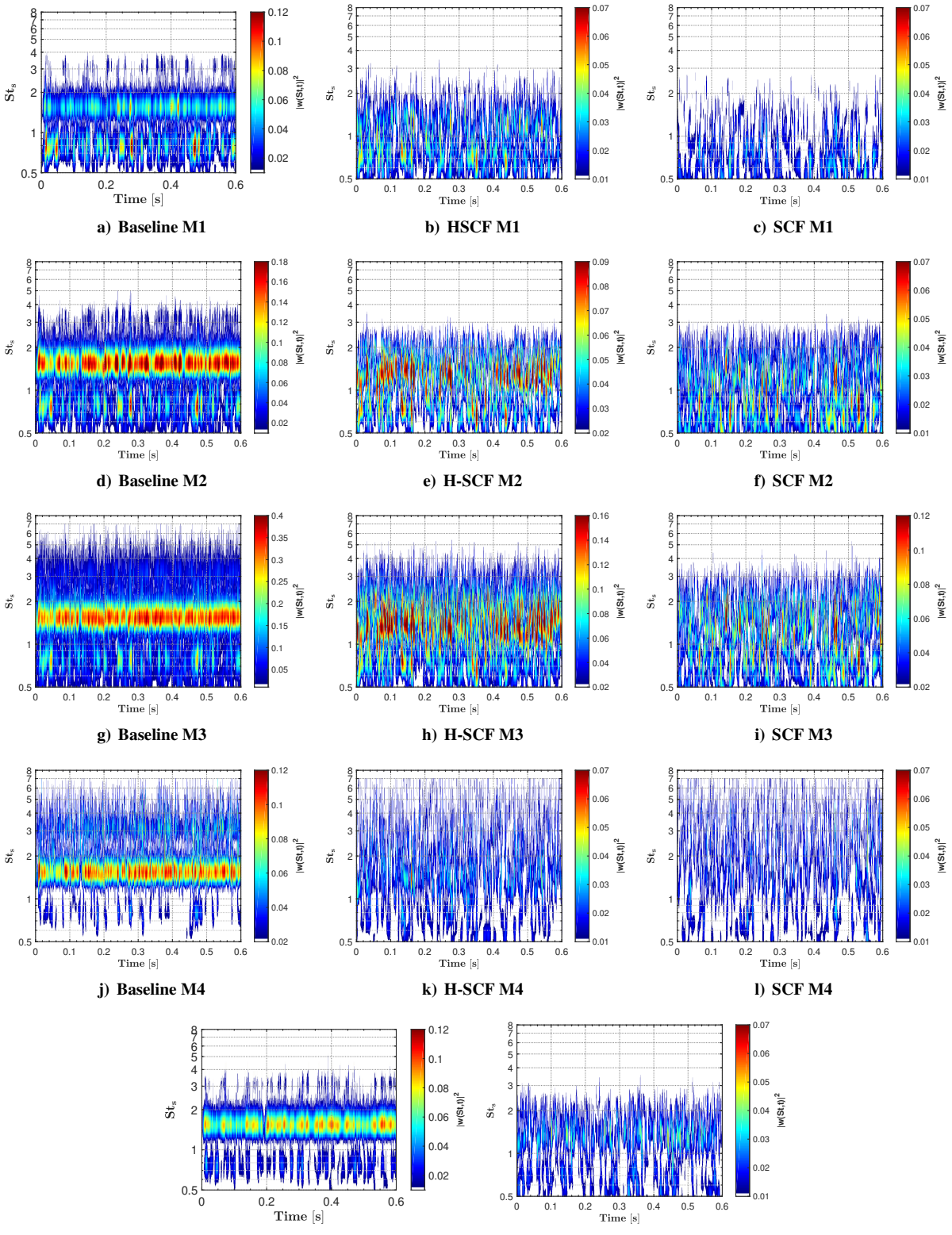

a) Baseline M1 b) HSCF M1 c) SCF M1

d) Baseline M2 e) H-SCF M2 f) SCF M2

g) Baseline M3 h) H-SCF M3 i) SCF M3

j) Baseline M4 k) H-SCF M4 l) SCF M4

m) Baseline S1 n) H-SCF S1

Fig. 12. Wavelet coefficient magnitude contours for the near-field remote sensors (M1-M4 and S1).

D. Wavelet analysis

The continuous wavelet transform (CWT) is used. The CWT consists of a signal projection over a basis of support functions provided by the translation and dilatation of a mother wavelet function. The definition, according to [51], is reported as follows:

$$w(s,t) = C_{\psi}^{\frac{-1}{2}} \int_{-\infty}^{\infty} p(\tau)\psi^*(\frac{t-\tau}{s}), \tag{8}$$

where s is the scale dilatation parameter corresponding to the width of the wavelet, τ is the translation parameter corresponding to the position of the wavelet, $C_{\psi}^{\frac{-1}{2}}$ is a constant that takes into account the mean value of $\psi(t)$ and $\psi^*(\frac{t-\tau}{s})$ is the complex conjugate of the dilated and translated mother wavelet $\psi(t)$. The Morlet kernel is chosen as the mother wavelet, as reported analytically in [52, 53].

The contours of the wavelet coefficient magnitude for the near-field remote sensors on the main-element M1-M4 and the slat S1 are presented in Fig. 12. The results for the Baseline configuration show a high wavelet coefficient at the vortex shedding frequency of $St_s = 1.61$ for all the remote sensor locations. For the frequency of interest, St_1 and St_2 highest wavelet coefficient can be found at location M3 amongst the various remote sensors. For the H-SCF and SCF configuration, the peak at St_2 is absent. The results show a high wavelet coefficient at M3 and a low wavelet coefficient at M4 compared to all the other remote sensor locations for all the tested configurations.

The wavelet coefficient of the frequencies of interest St_1 to St_6 (see Table 4) is extracted from the wavelet scalogram for further statistical analysis. The standard deviation of the extracted frequencies are presented in Fig. 13. The standard deviation results for the Baseline configuration at the primary frequency of interest at the spectral hump St_1 is highest for the remote sensor location M3. For the H-SCF and SCF configuration high values of the spectral hump St_1 can be observed at M3 compared to the other remote sensor locations. Since the main-element coherence results (M1-M4) also showed traces of the spectral hump for the H-SCF and SCF configuration, with high standard deviation at M3 for all the three configurations at St_1 it can be concluded that spectral hump arises from the slat gap.

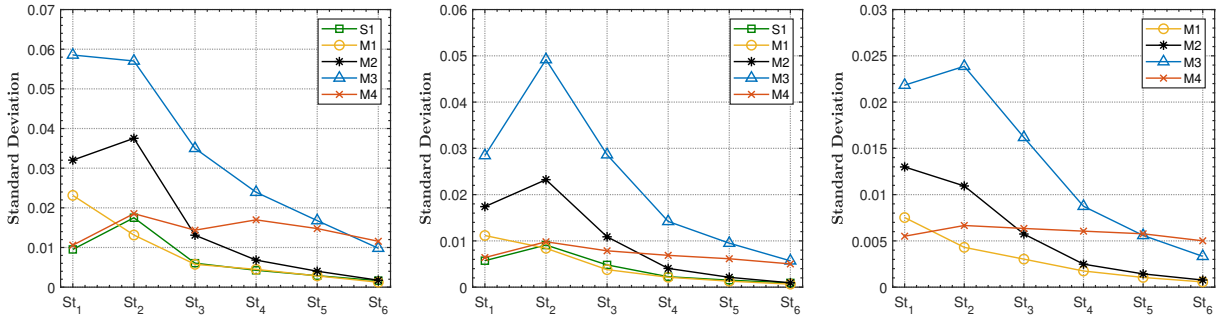

Fig. 13. Standard deviation of the extracted frequencies of interest (St_{1-6}) from the wavelet scalogram

IV. Conclusion

An experimental study with a 30P30N high airfoil fitted with two different types of slat cove fillers was carried out in the aeroacoustic facility at the University of Bristol. Unsteady surface pressure measurements within the slat cove were carried out using was 5 remote sensing transducers and 5 flush-mounted transducers. The results are presented for all the tested configurations at the angle of attack $\alpha = 18°$ for a free-stream velocity of $U_\infty = 30$ m/s, which corresponds to a chord-based Reynolds number of $Re_c = 7 \times 10^5$. As expected the slat cove filler configuration shows reduced noise levels at low frequency and the characteristic tonal noise generated by the slat is eliminated by the use of the slat cove fillers. Intermittent events induced by the resonant mechanism between the slat and its trailing edge were investigated for all the tested configurations. The streamwise correlation results between the remote sensors showed possible interference of the slat cove fillers with the turbulent structures making the cross-correlation shape larger probably due to the breaking of coherent structures. The streamwise coherence results showed that the spectral hump is different than that of the Rossiter modes. The coherence results for the SCF configuration also showed an increase at high frequency $St_s > 2$ between M1-M2, which requires further investigation. The near to far-field coherence results showed high coherence for the narrowband peaks for the Baseline configuration, whereas, the results for the slat cove filler configurations showed an overall low coherence. To identify the source of the spectral hump wavelet analysis

was carried out. The results from the wavelet analysis showed that high levels of wavelet coefficient for the frequency of interest was at the remote sensor location M3, which is located at the slat gap. Further analysis using standard deviation was carried out for the frequencies of interest extracted from the wavelet analysis. The results yet again confined that the source of the spectral hump was close to the slat gap region.

References

[1] Kamliya Jawahar, H., Theunissen, R., Azarpeyvand, M., and Carlos R.Ilario., "Flow characteristics of slat cove fillers", *Aerospace Science and Technology*, Vol. 100, May 2020, 105789.

[2] Kamliya Jawahar, H., Showkat Ali, S. A., Azarpeyvand, M., and Ilario, C., "Aerodynamic and aeroacoustic performance of high-lift airfoil fitted with slat cove fillers", *Journal of Sound and Vibration*, Vol. 479, 2020, 115347.

[3] Kamliya Jawahar, H., Azarpeyvand, M., and Carlos R.Ilario., "Aerodynamic and Aeroacoustic Performance of Three-element High Lift Airfoil fitted with Various Cove Fillers", AIAA 2018-3142, 2018.

[4] Kamliya Jawahar, H., Showkat Ali, S. A., Azarpeyvand, M., and Carlos R.Ilario., "Aeroacoustic Performance of Three-element High Lift Airfoil with Slat Cove Fillers", AIAA 2019-2440, 2019.

[5] Kamliya Jawahar, H., Azarpeyvand, M., and Carlos R.Ilario., "Numerical Investigation of High-lift Airfoil Fitted with Slat Cove Filler", AIAA 2019-2439, 2019.

[6] Kamliya Jawahar, H., Azarpeyvand, M., and Carlos R.Ilario. "Experimental Investigation of Flow Around Three-element High-lift Airfoil with Morphing Fillers", AIAA 2017-3364, 2017.

[7] Ai, Q., Kamliya Jawahar, H., and Azarpeyvand, M., "Experimental Investigation of Aerodynamic Performance of Airfoils Fitted with Morphing Trailing Edges", AIAA 2016-1563, 2016.

[8] Kamliya Jawahar, H., Ai, Q., and Azarpeyvand, M., "Experimental and Numerical Investigation of Aerodynamic Performance of Airfoils Fitted with Morphing Trailing Edges", AIAA 2017-3371, 2017.

[9] Kamliya Jawahar, H., Azarpeyvand, M., and Silva, C., "Aerodynamic and Aeroacoustic Performance of Airfoils Fitted with Morphing Trailing-edges", AIAA 2018-2815, 2018.

[10] Kamliya Jawahar, H., Ai, Q., and Azarpeyvand, M., "Experimental and Numerical Investigation of Aerodynamic Performance of Airfoils with Morphed Trailing Edges", *Renewable Energy*, Vol. 127, 2018, pp. 355-367.

[11] Showkat Ali, S. A., Azarpeyvand, M., and Ilario, C., "Trailing Edge Flow and Noise Control using Porous Treatments", *Journal of Fluid Mechanics*, Vol. 850, 2018, pp. 83-119.

[12] Showkat Ali, S. A., Szoke, M., Azarpeyvand, M., and Ilario, C., "Turbulent Flow Interaction with Porous Surfaces", AIAA 2018-2801, 2018.

[13] Showkat Ali, S. A., Azarpeyvand, M., Szoke, M. and da Silva, C. R. I., "Boundary layer flow interaction with a permeable wall," *Physics of Fluids*, Vol. 30, 2018, pp. 085111.

[14] Afshari, A., Azarpeyvand, M., Dehghan, A. A., and Szoke, M., "Trailing Edge Noise Reduction Using Novel Surface Treatments", AIAA 2016-2834, 2016.

[15] Liu, X., Kamliya Jawahar, H., Azarpeyvand, M., and Theunissen, R. "Aerodynamic Performance and Wake Development of Airfoils with Serrated Trailing Edges", *AIAA Journal*, Vol. 55, No. 11, 2017, pp. 3669-3680.

[16] Lyu, B., Azarpeyvand, M., and Sinayoko, S., "Prediction of Noise from Serrated Trailing Edges", *Journal of Fluid Mechanics*, Vol. 793, 2016, pp. 556-588.

[17] Mayer, Y. D., Lyu, B., Kamliya Jawahar, H., and Azarpeyvand, M., "A Semi-analytical Noise Prediction Model for Airfoils with Serrated Trailing Edges", *Renewable Energy (in press)*, 2019.

[18] Szoke, M., Fiscaletti, D., and Azarpeyvand, M., "Effect of Inclined Transverse Jets on Trailing-edge Noise Generation," *Physics of Fluids*, Vol. 30, 2018, pp. 085110.

[19] Olson, S., Thomas, F., and Nelson, R., "Mechanisms of Slat Noise Production in a 2D Multi-element Airfoil Configuration", AIAA 2001-2156, 2001.

[20] Khorrami, M., "Understanding Slat Noise Sources", Colloquium EUROMECH, Vol. 449, 2003.

[21] Kolb, A., Faulhaber, P., Drobietz, R., and Grunewald, M., "Aeroacoustic Wind Turbine Measurements on a 2D High-lift Configuration", AIAA 2007-3447, 2007.

[22] Mendoza, J. M., Brooks, T. F., and Humphreys, W. M., "An Aeroacoustic Study of a Leading Edge Slat Configuration", *International Journal of Aeroacoustics*, Vol. 1, No. 3, 2002, pp. 241-274.

[23] Hein, S., Hohage, T., Koch, W., and Schoberl, J., "Acoustic Resonances in a High-lift Configuration", *Journal of Fluid Mechanics*, Vol. 582, 2007, pp. 179-202.

[24] Murayama, M., Nakakita, K., Yamamoto, K., Ura, H., Ito, Y., and Choudhari, M., "Experimental Study of Slat Noise from 30P30N Three-element High-lift Airfoil in JAXA Hard-wall Low-speed Wind Tunnel", AIAA 2014-2080, 2014.

[25] Terracol, M., Manoha, E., and Lemoine, B., "Investigation of the Unsteady Flow and Noise Generation in a Slat Cove", *AIAA Journal*, Vol. 54, No. 2, 2016, pp. 469-489.

[26] Choudhari, M., and Lockard D. P., "Assessment of Slat Noise Predictions for 30P30N HighLift Configuration from BANC-III Workshop", AIAA 2015-2844 , 2015.

[27] Pagani, C. C., Souza, D. S., and Medeiros, M. F., "Slat Noise: Aeroacoustic Beamforming in Closed-section Wind Tunnel with Numerical Comparison", *AIAA Journal*, Vol. 54, No. 7, 2016, pp. 2100-2115.

[28] Pagani, C. C., Souza, D. S., and Medeiros, M. F., "Experimental Investigation on the Effect of Slat Geometrical Configuration on Aerodynamic Noise", *Journal of Sound and Vibration*, Vol. 394, 2017, pp. 256-279.

[29] Pascioni, K. A., and Cattafesta, L. N., "An Aeroacoustic Study of a Leading-edge Slat: Beamforming and Far-field Estimation using Near-field Quantities", *Journal of Sound and Vibration*, Vol. 429, 2018, pp. 224-244.

[30] Pascioni, K. A., and Cattafesta, L. N., "Unsteady Characteristics of a Slat-cove Flow-field", *Physical Review Fluids*, Vol. 3, 2018, pp. 1-27.

[31] Li, L., Liu, P., Guo, H., Hou, Y., Geng, X., and Wang, J., "Aeroacoustic Measurement of 30P30N High-lift Configuration in the Test Section with Kevlar Cloth and Perforated Plate", *Aerospace Science and Technology*, Vol. 70, 2017, pp. 590-599.

[32] Li, L., Liu, P., Guo, H., Geng, X., Hou, Y., and Wang, J., "Aerodynamic and Aeroacoustic Experimental Investigation of 30P30N High-lift Configuration", *Applied Acoustics*, Vol. 132, 2018, pp. 43-48.

[33] Li, L., Liu, P., Xing, Y., and Guo, H., "Time-frequency Analysis of Acoustic Signals from a High-lift Configuration with two Wavelet Functions", *Applied Acoustics*, Vol. 129, 2018, pp. 155-160.

[34] Li, L., Liu, P., Xing, Y., and Guo, H., "Wavelet Analysis of the Far-field Sound Pressure Signals Generated from a High-lift Configuration", *AIAA Journal*, Vol. 56, No.1, 2018, pp. 432-437.

[35] Horne, W. C., James, K. D., Arledge, T. K., Soderman, P. T., Field, M., Burnside, N., and Jaeger, S. M., "Measurement of 26%-scale 777 Airframe Noise in the NASA Ames 40-by-80 foot Wind Tunnel", AIAA 2005-2810, 2005.

[36] Streett, C., Casper, J., Lockard, D., Khorrami, M., Stoker, R., Elkoby, R., Wenneman, W., and Underbrink, J., "Aerodynamic Noise Reduction for High-lift Devices on a Swept Wing Model", AIAA 2006-212, 2006.

[37] Andreou, C., Graham, W., and Shin, H. C., "Aeroacoustic Study of Airfoil Leading Edge High-lift Devices", AIAA 2006-2515, 2006.

[38] Andreou, C., Graham, W., and Shin, H. C., "Aeroacoustic Comparison of Airfoil Leading Edge High-lift Geometries and Supports", AIAA 2007-230, 2007.

[39] Imamura, T., Ura, H., Yokokawa, Y., Enomoto, S., Yamamoto, K., Hirai, T., Group, A. P., and Division, E. S., "Designing of Slat Cove Filler as a Noise Reduction Device for Leading-edge Slat", AIAA 2007-3473, 2007.

[40] Ura, H., Yokokawa, Y., Imamura, T., Ito, T., and Yamamoto, K., "Investigation of Airframe Noise from High Lift Configuration Model", AIAA 2008-19, 2008.

[41] Shmilovich, A., Yadlin, Y., and Pitera, D. M., "Wing Leading-edge Concepts for Noise Reduction", 27th International Congress of the Aeronautical Sciences, ICAS 2010-5.2.2, 2010.

[42] Shmilovich, A., Yadlin, Y., and Company, T. B., "High-lift Systems for Enhanced Take-off Performance", 28th International Congress of the Aeronautical Sciences, 2012, pp. 1-13.

[43] Scholten, W. D., Hartl, D. J., Turner, T. L., and Kidd, R. T., "Development and Analysis-Driven Optimization of Superelastic Slat-cove Fillers for Airframe Noise Reduction", *AIAA Journal*, Vol. 54, No. 3, 2016, pp. 1078-1094.

[44] Tao, J., and Sun, G., "A Novel Optimization Method for Maintaining Aerodynamic Performances in Noise Reduction Design", *Aerospace Science and Technology*, Vol. 43, 2015, pp. 415-422.

[45] Zhang, Y., Neill, A., and Cattafesta, L. N., "Assessment of Noise Reduction Concepts for Leading-Edge Slat Noise", AIAA 2018-3461, 2018.

[46] Mayer, Y., Kamliya Jawahar, H., Szoke, M., Ali, S. A. S., and Azarpeyvand, M., "Design and Performance of an Aeroacoustic Wind Tunnel Facility at the University of Bristol", *Applied Acoustics*, Vol. 155, 2019, pp. 358-370.

[47] Garcia-Sagrado, A. and Hynes, T., "Wall Pressure Sources Near an Airfoil Trailing Edge under Turbulent Boundary Layers", *Journal of Fluids and Structures*, Vol. 30, 2012, pp. 3-34.

[48] Liu, X., "Aerodynamic and Wake Development of Aerofoils with Trailing-Edge Serrations", University of Bristol, PhD Thesis, 2018.

[49] Rossiter, J., "Wind Tunnel Experiments on the Flow Over Rectangular Cavities at Subsonic and Transonic Speeds", Royal Aircraft Establishment ARC R&M 3238, 1966.

[50] Meloni S., Di Marco A., Mancinelli M., Camussi R., "Wall pressure fluctuations induced by a compressible jet flow over a flat plate at different Mach numbers", *Exp Fluids*, Vol. 60, 2019.

[51] Meloni S., Di Marco A., Camussi R. , Mancinelli M. (2019) “Parametric characterization of wall pressure fluctuations induced by a compressible jet flow interacting with a flat plate”, AIAA 2019-2711.

[52] Morlet, J., “Sampling Theory and Wave Propagation”, in: Proceedings of the 51st Annual Meeting of the Society Exploration Geophysics, 1981.

[53] Jordan P., Jaunet V., Towne A., Cavalieri A., Colonius T., Schmidt O., Agarwal A., “Jet–flap interaction tones”, *Journal of Fluid Mechanics*, Vol. 853, 2018, pp. 333-358.

[54] Mancinelli, M., Pagliaroli, T., Camussi, R., Castelain, T., “On the hydrodynamic and acoustic nature of pressure proper orthogonal decomposition modes in the near field of a compressible jet”, *Journal of Fluid Mechanics*, Vol. 836, 2018, pp. 998-1008.